





# Combination of a novel heat shock protein 90-targeted photodynamic therapy with PD-1/PD-L1 blockade induces potent systemic antitumor efficacy and abscopal effect against breast cancers

Kensuke Kaneko,<sup>1</sup> Chaitanya R Acharya ,<sup>1</sup> Hiroshi Nagata,<sup>1</sup> Xiao Yang,<sup>1</sup> Zachary Conrad Hartman ,<sup>1</sup> Amy Hobeika,<sup>1</sup> Philip F Hughes,<sup>2</sup> Timothy A J Haystead,<sup>2</sup> Michael A Morse,<sup>3</sup> Herbert Kim Lyerly ,<sup>1</sup> Takuya Osada <sup>1</sup>

**To cite:** Kaneko K, Acharya CR, Nagata H, *et al.* Combination of a novel heat shock protein 90-targeted photodynamic therapy with PD-1/PD-L1 blockade induces potent systemic antitumor efficacy and abscopal effect against breast cancers. *Journal for ImmunoTherapy of Cancer* 2022;**10**:e004793. doi:10.1136/jitc-2022-004793

► Additional supplemental material is published online only. To view, please visit the journal online (<http://dx.doi.org/10.1136/jitc-2022-004793>).

Accepted 07 September 2022



© Author(s) (or their employer(s)) 2022. Re-use permitted under CC BY-NC. No commercial re-use. See rights and permissions. Published by BMJ.

<sup>1</sup>Department of Surgery, Duke University Medical Center, Durham, North Carolina, USA

<sup>2</sup>Department of Pharmacology and Cancer Biology, Duke University, Durham, North Carolina, USA

<sup>3</sup>Department of Medicine, Duke University Medical Center, Durham, North Carolina, USA

## Correspondence to

Dr Takuya Osada;  
osada001@duke.edu

## ABSTRACT

**Background** We previously demonstrated potent antitumor activity against human breast cancer xenografts using photodynamic therapy (PDT) targeting a novel tumor-specific photosensitizer (HS201), which binds heat shock protein 90 (HS201-PDT). However, induction of systemic antitumor immunity by HS201-PDT alone or by the combination strategy with immune checkpoint blockade has yet to be determined.

**Methods** Using unilateral and bilateral implantation models of syngeneic breast tumors (E0771, MM3MG-HER2, and JC-HER3) in mice, we assessed whether HS201-PDT could induce local and systemic antitumor immunity. In an attempt to achieve a stronger abscopal effect for distant tumors, the combination strategy with anti-PD-L1 antibody was tested. Tumor-infiltrating leukocytes were analyzed by single cell RNA-sequencing and receptor-ligand interactome analysis to characterize in more detailed the mechanisms of action of the treatment and key signaling pathways involved.

**Results** HS201-PDT demonstrated greater tumor control and survival in immune competent mice than in immunocompromised mice, suggesting the role of induced antitumor immunity; however, survival was modest and an abscopal effect on distant implanted tumor was weak. A combination of HS201-PDT with anti-PD-L1 antibody demonstrated the greatest antigen-specific immune response, tumor growth suppression, prolonged mouse survival time and abscopal effect. The most significant increase of intratumoral, activated CD8+T cells and decrease of exhausted CD8+T cells occurred following combination treatment compared with HS201-PDT monotherapy. Receptor-ligand interactome analysis showed marked enhancement of several pathways, such as CXCL, GALECTIN, GITRL, PECAM1 and NOTCH, associated with CD8+T cell activation in the combination group. Notably, the expression of the CXCR3 gene signature was the highest in the combination group, possibly explaining the enhanced tumor infiltration by T cells.

## WHAT IS ALREADY KNOWN ON THIS TOPIC

⇒ The Hsp90-targeted photosensitizer, HS201, accumulates in aggressive breast cancers in vivo, and photodynamic therapy using laser light applied to tumors following HS201 administration (HS201-photodynamic therapy, PDT) showed direct antitumor efficacy against human breast cancer xenografts with various molecular and clinical subtypes.

## WHAT THIS STUDY ADDS

⇒ In the current study, we demonstrated that HS201-PDT could induce tumor-antigen specific cellular immunity that resulted in an abscopal effect at the site of distant tumors and prolonged survival in murine syngeneic breast cancer models.

⇒ The antitumor efficacy of HS201-PDT was enhanced by systemic delivery of anti-PD-L1 antibody.

⇒ Tumor infiltration with activated CD8+T cells was enhanced in PDT treated tumors as well as in distant untreated tumors following the combination of HS201-PDT and anti-PD-L1.

⇒ scRNA-seq analysis of tumor infiltrating leukocytes revealed enhanced communications between CD8 T cells and macrophages in the tumors treated with the combination therapy. Elements of the CXCR3 gene signature were strongly upregulated in CD8 T cells and macrophages, thus serving as a potential biomarker of antitumor immunity in HS201-PDT treated tumors.

## HOW THIS STUDY MIGHT AFFECT RESEARCH, PRACTICE OR POLICY

⇒ This study demonstrates the potential of combined Hsp90-targeted PDT and PD-1/PD-L1 blockade in breast cancer immunotherapy and the CXCR3 gene signature as a surrogate marker for the clinical activity of the treatment. Further preclinical and clinical studies to assess this combined therapy are warranted.

**Conclusions** The increased antitumor activity and upregulated CXCR3 gene signature induced by the combination of anti-PD-L1 antibody with HS201-PDT warrants the clinical testing of HS201-PDT combined with PD-1/PD-L1 blockade in patients with breast cancer, and the use of the CXCR3 gene signature as a biomarker.

## BACKGROUND

Application of immunotherapy to breast cancer (BC) has received considerable attention<sup>1</sup>; however, anti-PD-1/PD-L1 antibodies that have revolutionized treatment of some malignancies have modest activity only in a subset of individuals with triple-negative BC (TNBC).<sup>2–5</sup> Defects in the tumor microenvironment (TME) including (1) decrease in number and activity of cytotoxic CD8+T cells, (2) decrease in dendritic cell maturation and trafficking, (3) increase of immunosuppressive cells, such as regulatory T (Treg) cells, tumor-associated macrophages (TAMs), and myeloid derived suppressor cells, that produce inhibitory molecules, such as IL-6, IL-10, TGF- $\beta$  and VEGF, and (4) increased expression level of PD-L1 by tumor cells and antigen-presenting cells, are thought to be responsible for this limited efficacy.<sup>6,7</sup> T cell trafficking depends on the release of chemokines Cxcl9/10/11 in the target tissue, which then bind to Cxcr3 on T cells.<sup>8–10</sup> CXCL9 is associated with immune infiltration and favorable prognosis in ER-negative BC.<sup>11</sup> CXCR3 signaling is important in the maintenance of an inflamed TME<sup>12</sup> and lack of CXCR3 signaling was shown to increase M2 polarization of TAM in murine BC.<sup>13</sup> Our goal was to increase the chemokine expression at the site of TNBCs, Cxcr3 expression on effector T cells, and stronger antigen-presenting cell to T cell signaling to synergize with anti-PD-1/PD-L1 therapy.

Strategies proposed to overcome immune deficits in the TME include (1) local administration of oncolytic viruses, (2) local administration of immune-stimulatory reagents such as interleukin-2 (IL-2), IL-12, Toll-like receptor agonists and Stimulator of Interferon Gene agonists, (3) radiotherapy, and (4) physical therapies such as electrochemotherapy, high-intensity focused ultrasound (HIFU), photothermal therapy and hyperthermia.<sup>14–21</sup> For example, we recently showed that mechanical disruption of tumor tissue using HIFU modified the TME, by repolarizing macrophages to an M1-like phenotype and inducing intratumoral infiltration of CD8+T cells, and elicited strong systemic antitumor immunity.<sup>22</sup> In common, these approaches seek to either activate more potent effector T cells or modify the TME to allow intratumoral T cell migration; however, few effectively enhance the signals for T cell infiltration. Another tumor ablative approach is photodynamic therapy (PDT) which consists of systemic administration of a photosensitizer compound followed by application of laser light resulting in the generation of reactive oxygen species that damages the target cells. We have developed a novel photosensitizer HS201, which consist of verteporfin (VP) tethered to a heat shock protein 90 (Hsp90) small molecule inhibitor, that selectively accumulates within tumors, permitting targeted

PDT (HS201-PDT).<sup>23</sup> HS201-PDT showed a significant antitumor effect against various human BC xenografts including aggressive BCs implanted in immunocompromised mice. Others have reported that conventional PDT can enhance the immune response to tumors.<sup>24,25</sup> However, the systemic antitumor effect of HS201-PDT has not been determined in immunocompetent models.

In the current study, we investigated the capacity of HS201-PDT with/without immune checkpoint blockade (ICB) to induce antitumor immunity and antitumor efficacy in ER-negative murine BCs in immunocompetent mice. We demonstrated that combination treatment of HS201-PDT and anti-PD-L1 antibody could induce significantly stronger systemic antitumor immunity and an abscopal effect, which refers to tumor regression at a location distant from the primary treatment site, compared with HS201-PDT or anti-PD-L1 monotherapy. Using transcriptome analysis of tumor specimens, we further demonstrated that the combination treatment upregulated expression of the CXCR3 gene signature associated with a higher frequency of activated CD8 T cells and fewer M2 macrophages compared with HS201-PDT monotherapy.

## METHODS

### Cell culture

E0771 cells, a mammary adenocarcinoma cell line derived from a C57Bl/6J mouse, were lentivirally transfected with ovalbumin (E0771-OVA). MM3MG-HER2 cells were established from murine mammary epithelial MM3MG cells as previously described.<sup>26</sup> JC-HER3 cells were established by lentiviral transfection of HER3 to JC murine BC cell line.<sup>27</sup> HER2 or HER3-positive transfected cells were sorted by flow cytometry and used for in vitro and in vivo experiments. E0771 cells and JC-HER3 cells were used as TNBC models<sup>28</sup> and MM3MG-HER2 as a HER2+BC model. Cells were maintained in Dulbecco's Modified Eagle's (DMEM) medium supplemented with 10% heat-inactivated fetal bovine serum (FBS) and penicillin/streptomycin at 37°C in a humidified incubator containing 5% CO<sub>2</sub>.

### Reagents and antibodies

HS201, a novel photosensitizer made of VP (Novartis Pharmaceuticals, Basel, Switzerland) tethered to an Hsp90 small molecule inhibitor (HS10), was used for in vitro and in vivo imaging and PDT. HS201 was developed and supplied by Haystead Lab (Department of Pharmacology and Cancer Biology, Duke University) as previously described.<sup>23</sup> Anti-PD-L1 antibody (clone; 10F.9G2) was purchased from Bio X cell (New Hampshire USA) and used for animal treatment. Annexin V-Allophycocyanin was purchased from BD Biosciences (California USA) and 7-AAD from Beckman Coulter Inc. (California, USA). Detailed information of antibodies used for flow cytometry is shown in online supplemental methods.

## Mice

Inbred BALB/c and C57BL6 mice were purchased from Jackson Laboratory, Bar Harbor, USA. Inbred severe combined immunodeficiency (SCID) Beige mice were purchased from Taconic Biosciences New York USA, and bred at Duke University Cancer Center Isolation Facility (CCIF). Human HER3 transgenic mice were generated as previously described<sup>27</sup> and maintained at CCIF. All animal studies described were approved by the Duke University Medical Center Institutional Animal Care & Use Committee and the US Army Medical Research and Materiel Command Animal Care and Use Review Office and performed in accordance with guidelines published by the Commission on Life Sciences of the National Research Council.

## In vitro measurement of cellular reagents uptake

The in vitro uptake of reagents designed for NIR imaging and PDT was measured using Odyssey CLx imaging system (LI-COR, Inc. Nebraska USA) at 700 nm wavelength. BC cells were seeded in 96-well plates (10,000 cells/well) and cultured in DMEM media with 10% FBS at 37°C. After the cells reached sub confluent in each well, HS201 (0.03–10 μM, respectively) was added, incubated for 30 min, removed, and washed by phosphate buffered saline (PBS) once. Signal intensity of each well was measured at 700 nm to evaluate cellular uptake of HS201.

## Flow cytometry analysis

For the analysis of tumor infiltrating lymphocytes, tumors were minced with surgical blade and digested with triple enzyme buffer (type III collagenase, hyaluronidase, DNase) for 1.5 hour at 37°C. Cells were washed with PBS, stained with LIVE/DEAD Fixable Aqua Dead Cell Stain Kit (Thermo Fisher Scientific, Rockford, Illinois, USA), and followed by intracellular staining and/or cell surface staining as previously described.<sup>22 23 26</sup> Detailed staining methods are shown in online supplemental methods. Cells were acquired by LSRII flow cytometer (BD Biosciences, San Jose, California, USA) and analyzed by FlowJo software IX (BD Biosciences). Red laser (633 nm wavelength) was used for excitation and signals were detected with filter 710/50 nm.

## Photodynamic therapy

BC cells ( $1 \times 10^6$  cells /mouse) were injected into the right flank of female mice. After the tumor size reached 8 mm in diameter, PDT was performed as we previously reported.<sup>23</sup> First, HS201 (25 nmol/mouse) was administered via tail vein injection. Six hours after the injection of photosensitizer, laser at a wavelength of 690 nm was irradiated to the tumors at the dose of 120 J/cm<sup>2</sup> (500 mW/cm<sup>2</sup>/4 min) using medical laser system ML7710 (Modulight, Tampere, Finland). The laser irradiation was repeated at 24 hours after the injection of HS201 as previously reported.<sup>23</sup> In vivo imaging was performed in the same way as described above. Sample sizes for each group in each experiment are shown in online supplemental methods. Tumor size

was monitored by caliper measurement twice a week. Tumor volume was calculated as follows: tumor volume (mm<sup>3</sup>)=width (mm)×width (mm)×length (mm)/2.

## IFN-γ ELISPOT

Mouse IFN-γ ELISPOT assays (Mabtech, Cincinnati, Ohio, USA) were done according to the manufacturer's instructions as previously described.<sup>22 27</sup> Overlapping HER2 or HER3 mixed peptides (JPT Peptide Technologies, Berlin, Germany) or OVA257-264 (SIINFEKL) peptide were used to detect anti-HER2, anti-HER3 or anti-OVA cellular responses. HIV peptide mix (BD Bioscience) was used as a negative control of the assay. A detailed method is shown in online supplemental methods.

## Antibody detection in serum

The amount of serum antibodies specific to the target antigen were assessed by either ELISA (OVA) or cell-based ELISA (HER2 and HER3) as previously described.<sup>22 27</sup> Briefly, ELISA for anti-OVA antibodies in serum was performed using OVA protein (2.5 μg/50 μL/well) coated plates (Immulon 4HBX, Thermo Scientific, Massachusetts, USA). Cell-based ELISA was performed using 96-well plates seeded with BC cells (4T1-HER2, 4T1-HER3, or parental 4T1, 10,000 cells/well). IRDye 800CW Donkey anti-mouse IgG antibody (1:2000 in 1% BSA-PBS, LI-COR Biosciences, Lincoln, Nebraska, USA) was added and plates were analyzed using LI-COR ODYSSEY imager (LI-COR). Detailed methods are shown in online supplemental method.

## Immunohistochemistry

Formalin-fixed paraffin embedded tissues were cut into 4 μm sections and stained with anti-CD4 (1:100, D7D2Z, Cell Signaling Technology, Danvers, Massachusetts, USA) or anti-CD8 mAb (1:400, D4W2Z, Cell Signaling) by the HRP method, followed by standard chromogenic immunohistochemistry protocol. A detailed method is shown in online supplemental methods. Stained slides were scanned on a DP80 microscope (OLYMPUS, Tokyo, Japan) and digital images were viewed using cellSens (OLYMPUS). CD4+T cells and CD8+T cells were counted in randomly selected five different high-power fields to obtain an average number for each condition.

## Single cell RNA-seq analysis

Single-cell suspensions enzymatically dissociated from untreated or treated tumors 7 days after treatment initiation were obtained as mentioned above. The CD45+leukocytes were sorted from the tumor digest suspensions by flow cytometry, and 10X libraries were created using Chromium Single Cell 5' Library Construction Kits (V.1.1) (10X Genomics, Pleasanton, California, USA) following manufacturer's protocol. Both gene expression (GEX) and V(D)J enrichment libraries were created for each sample. Generated cDNA and final GEX/T cell receptor (TCR) libraries were quality checked using an Agilent Bioanalyzer 2100 and submitted to MedGenome Inc (Foster City, California, USA) for sequencing on a NovaSeq S4 instrument. Fastq



files from 10X library sequencing were processed using Partek Genomics Suite software (V.9.0.20, Copyright ; 2018 Partek). Sequences were aligned to the mm10 reference genome (STAR aligner V.2.6.1). Deduplicated unique molecular identifier (UMI) counts were filtered using Seurat (V.4.0.6)<sup>29</sup> to include cells with (1) total reads between 200 and top 95th percentile of expression distribution, and (2) genes with a maximum of 10% mitochondrial reads. After log-normalizing individual datasets, data were scaled after regressing out total number of UMI counts, percent mitochondrial GEX and cell-cycle phase in order to account for the variability in GEX. We then rank genes by the number of datasets they appear in (breaking ties by the median rank across datasets) and picked top 5000 genes that can be used for data integration using Seurat integration workflow. Scaled z-scores for each gene within the integrated data were calculated, which were later used as input to principal component analysis. Variable TCR and immunoglobulin genes along with ribosomal and mitochondrial genes were removed from the list of variable genes to prevent clustering based on variable V(D)J transcripts, ribosomal and mitochondrial content. Clusters, identified using shared nearest neighbor-based clustering on the basis of the first 30 principal components, were visualized using UMAP<sup>30</sup> plots using first 10 principal components, a minimum distance of 0.5 and 75 nearest neighbors. Ligand-receptor (LR) interactions between any two cell types were interrogated drawing from a curated list of LR pairs using CellChat (version 1.1.3).<sup>31</sup> P values for each LR interaction were computed by randomly permuting the cell type labels and statistical significance was called at 5% false discovery rate (FDR). Significant LR interactions were visualized using chord diagrams (circus plots) and heatmaps.

T cell diversity was calculated using Shannon's entropy ( $H$ ) as follows;  $H = - \sum_{i=1}^S P_i \ln(P_i)$

$S$  is the number of clones and  $P$  is the proportion of each clone within the repertoire.  $P = n$  (read count of each individual clone)/ $N$  (the sum of all reads in the repertoire).<sup>32</sup> T cell clonality was calculated as follows; clonality index =  $1 - \text{Shannon entropy} / \ln(N)$ .  $N$  is the number of clonotypes for each sample.

### Statistical analysis

Tumor volumes, flow cytometry, ELISA, and ELISPOT data from experiments with three or more treatment groups were analyzed by One-way analysis of variance with Tukey's multiple comparisons test. A two-tailed, unpaired Student's t-test was used for experiments with only two groups. Tumor volumes were analyzed at the terminal endpoint only, unless otherwise indicated. Statistical analyses were performed using Prism (GraphPad, San Diego, California, USA). Kaplan-Meier survival curves for tumor-bearing mice were generated and log-rank tests were performed using Prism. P values of 0.05 or less were considered statistically significant and shown in the graphs. \* $p < 0.05$ ; \*\* $p < 0.01$ ; \*\*\* $p < 0.001$ .

## RESULTS

### HS201 accumulates in murine BC cells and leads to cell killing after application of PDT

We first demonstrated the uptake of HS201 by triple-negative E0771 cells was concentration-dependent (online supplemental figure 1A). Further, we observed that killing of E0771 by HS201 in combination with laser light was both HS201 concentration-dependent and light energy dose-dependent (online supplemental figure 1B). This cell killing was predominantly apoptotic (online supplemental figure 1C).

Next, we confirmed the HS201 accumulated in murine syngeneic E0771 breast tumors in vivo. As shown in online supplemental figure 2A, strong nIR signals were confirmed in E0771 tumors, compared with non-tumor background areas. The nIR signal level peaked at 12 hours after administration of HS201, then gradually decreased till day 6 (online supplemental figure 2B), as we observed in human BC xenografts grown in immunodeficient SCID beige mice.<sup>23</sup> Six hours after HS201 injection, there was significant accumulation of HS201 in harvested E0771 tumor tissue (online supplemental figure 2C), and specifically within individual tumor cells (online supplemental figure 2D). These data confirm that E0771 cells efficiently take up HS201 in vivo and can be killed by HS201-PDT.

### HS201-PDT-induced significant tumor growth suppression of E0771 murine BC without survival benefit in immunocompromised mice

To evaluate the antitumor effect of PDT without the influence of immune response, we tested in vivo PDT using E0771 tumors in immunocompromised SCID beige mice (lacking B, T cells and NK cell functions). Based on the previous optimization of HS201-PDT,<sup>23</sup> HS201 was administered at the dose of 25 nmol/mouse via tail vein injection, and laser irradiation ( $120 \text{ J/cm}^2$ ) to the tumors were repeated twice (Drug-Light Interval: 6 hours and 24 hours) as shown in the schema (figure 1A). As expected, HS201-PDT group had the strongest tumor growth suppression, however, tumor growth in this group accelerated at later time points (figure 1B). HS201 injection alone or Laser irradiation alone did not significantly suppress the growth of E0771 breast tumors, thus confirming the need for both photosensitizers and light in the tumoricidal effect of HS201-PDT.

Although the mice in HS201-PDT treatment group tended to survive longer than untreated mice, there was no statistically significant difference (figure 1C). These data suggest that in the absence of B, T and NK cells, HS201-PDT has modest antitumor effect in vivo.

### HS201-PDT-induced significant tumor growth suppression of E0771 murine BC with survival benefit in immunocompetent mice

Having observed that the HS201-PDT only modestly affected survival of immune-incompetent mice implanted with E0771, we wanted to determine whether the outcome would be improved by the presence of antitumor

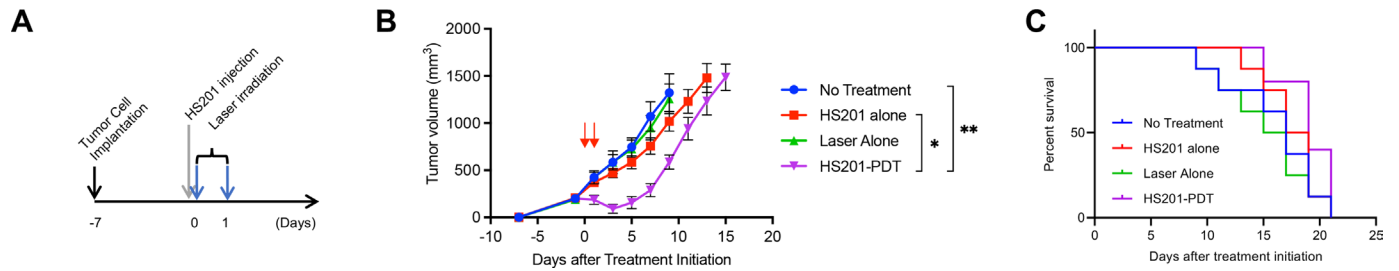


**Figure 1** Antitumor effect of HS201-PDT against E0771 tumors in immunodeficient mice. (A) Treatment schedule of HS201-PDT. When the size of the E0771 tumor reached approximately 8 mm in diameter, HS201 (25 nmol/mouse) was administered to the mice via tail vein injection, and laser (690 nm wavelength, 120 J/cm<sup>2</sup>) was irradiated to tumor area with DLI of 6 and 24 hours. Tumor size was monitored until the volume reach over 2000 mm<sup>3</sup>. (B) Antitumor Effect of HS201-PDT against E0771 tumor in immunocompromised SCID beige mice. HS201-PDT was carried out according to the schedule shown in figure 2A (laser irradiation indicated with red arrows). As controls, no treatment group, HS201 injection alone, and laser irradiation alone were made. The data shown are mean±SEM of tumor volumes (n=5 for HS201-PDT group and n=8 for other groups). Statistical analysis was performed for the tumor volume on day 9. (C) Overall survival of E0771 tumor-bearing SCID beige mice treated with HS201-PDT. Mice (n=5 for HS201-PDT group and n=8 for other groups) were counted as dead when tumor volume reached humane endpoint according to IACUC approved protocol (>2000 mm<sup>3</sup>). PDT, photodynamic therapy; DLI, drug-light interval; IACUC, Institutional Animal Care and Use Committee; SCID, severe combined immunodeficiency.

immunity. In immunocompetent E0771-bearing C57BL/6 mice, HS201-PDT of the implanted tumor significantly suppressed tumor growth and prolonged overall survival compared with no treatment (figure 2A,B). To confirm the antitumor activity was antigen-specific, we applied HS201-PDT treatment to established E0771 tumors expressing the model antigen OVA (E0771-OVA) and analyzed the splenocytes and serum to assess cellular and humoral immune responses against OVA. OVA-specific cellular immune response was only observed in HS201-PDT treated mice, but not in untreated mice (figure 2C). ELISA showed comparable levels of anti-OVA antibody in the sera of both groups (figure 2D). These results suggest that the cellular immunity played a major role in HS201-PDT-induced antitumor effects. To study the local cellular response in more detail, we analyzed digested tumor by flow cytometry. We observed a decrease of CD4+Foxp3<sup>+</sup> regulatory T cells, and increases of the CD8/CD4 and the CD8/CD4+Foxp3<sup>+</sup>CD25<sup>+</sup> Treg ratios, suggesting HS201-PDT favorably alters the TME (figure 2E).

### HS201-PDT induces a weak abscopal effect

Having confirmed induction of systemic antitumor immunity by HS201-PDT in immunocompetent mice, we wished to test whether this immunity could suppress the growth of distant, implanted but untreated, tumors. Using a bilateral tumor model of E0771 tumors in C57BL/6 mice, tumors in the right flank were treated or untreated with HS201-PDT, and tumor growth of the untreated contralateral flank tumors was monitored. As shown in figure 2F, HS201-PDT induced significant tumor growth suppression for the treated tumors in the right flank; however, the sizes of distant implanted tumors (left flank) were minimally reduced (p=0.10) compared with untreated mice (figure 2F).

### HS201-PDT combined with checkpoint blockade induced stronger antitumor immunity and tumor growth suppression

Although we observed local and systemic immunity induced by HS201-PDT of implanted tumors, tumors continued to grow and were eventually lethal (figure 2A,B). We hypothesized that this is due to T cell exhaustion in the TME. Given this hypothesis, we sought to determine if combining immune checkpoint inhibition to HS201-PDT could maintain the activation of cytotoxic T cells and enhance the anti-tumor efficacy. Therefore, E0771 tumor-bearing mice were treated by HS201-PDT, anti-PD-L1 antibody or both as shown in figure 3A. Although HS201-PDT was again noted to suppress tumor growth which was marginally enhanced by anti-PD-L1 (figure 3B), only the combination resulted in statistically significant prolongation of survival compared with untreated mice (figure 3C). Importantly, the combination statistically prolonged survival compared with anti-PD-L1 alone, suggesting that the local PDT-based therapy enhances the efficacy of anti-PD-L1 therapy.

### Combination of HS201-PDT and checkpoint blockade enhanced antigen-specific immune response against MM3MG-HER2 tumors

Here, we sought to validate the efficacy of the combination treatment using MM3MG-HER2, another BC model which is driven by the well-known oncogene HER2.<sup>26</sup> MM3MG-HER2 tumor-bearing BALB/c mice were treated with the same schedule of HS201-PDT and ICB as described in figure 3A. Significant tumor growth suppression and tumor rejection were observed in HS201-PDT monotherapy and the combination treatment groups, but not in anti-PD-L1 monotherapy groups (figure 3D). Although tumors were eradicated by HS201-PDT monotherapy in 6 mice out of 8 mice (75%), the combination treatment eradicated tumors in 100% of the mice by day 7 after the treatment, while no mouse in the control or

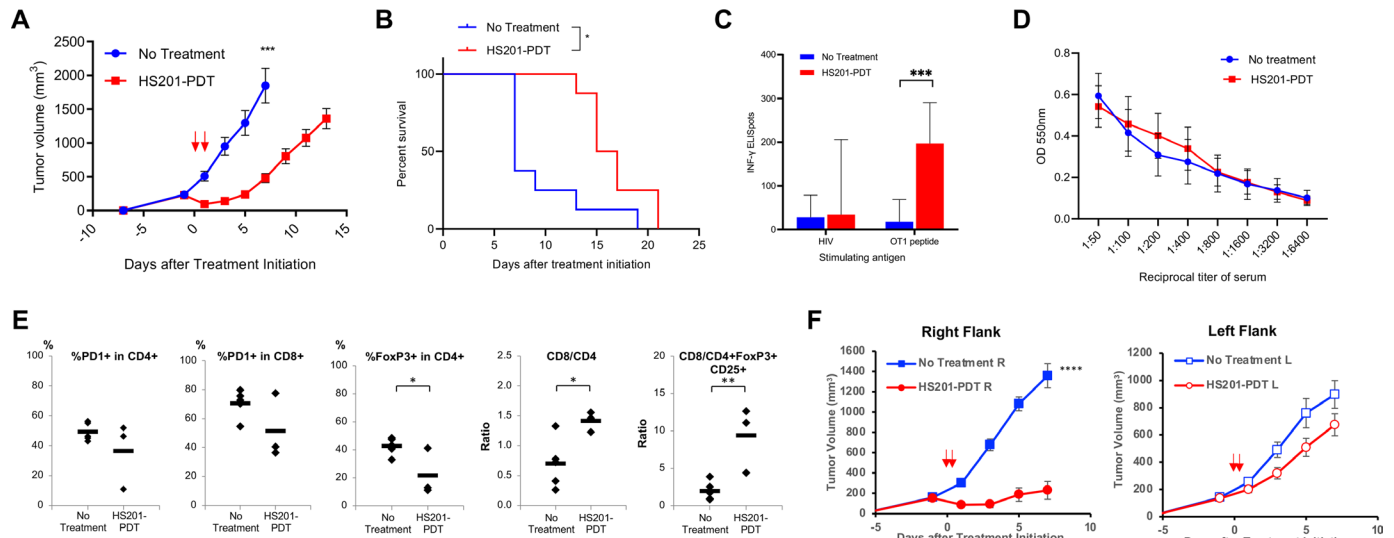


**Figure 2** HS201-PDT induced improved antitumor effect and prolonged survival against E0771 tumors in immunocompetent mice. (A) Antitumor effect of HS201-PDT against E0771 tumor in immunocompetent C57BL/6 mice. E0771 cells ( $1 \times 10^6$  cells/mouse) were subcutaneously injected to the flank of female C57BL/6 mice. As shown in figure 1A, HS201-PDT was carried out according to the schedule shown in figure 2A (laser irradiation indicated with red arrows). Mice in a control group received no treatment. The data shown are mean  $\pm$  SEM of tumor volumes ( $n=8$  for each group). Statistical analysis was performed for the tumor volume on day 7. (B) Overall survival of E0771 tumor-bearing immunocompetent mice treated with HS201-PDT. Survival curves of E0771 tumor-bearing C57BL/6 mice in each group are shown ( $n=8$  for each group). Mice were counted as dead when tumor volume reached humane endpoint according to IACUC Approved protocol. (C) Antigen-specific cellular immune response induced by HS201-PDT in immunocompetent mice. E0771-OVA tumors grown in C57BL/6 mice were untreated or treated with HS201-PDT. Ten days after the initiation of HS201-PDT, all mice were euthanized and spleen and blood samples were collected for the assays. Splenocytes were tested for OVA-specific cellular immune response by IFN- $\gamma$  ELISPOT assay, using OT1 specific peptide (SIINFEKL) or control HIV peptide mix as stimulating antigens. The number of IFN- $\gamma$  positive spots per 500k splenocytes is shown. ELISpot count obtained without stimulating antigen was subtracted from the other ELISpot counts as a background. Data are shown as mean  $\pm$  SD  $n=8$  for each group. (D) Humoral immune response induced by HS201-PDT in immunocompetent mice. OVA-specific antibody production was tested by ELISA. Mouse serum were titrated (1:50–1:6400 dilution) and applied to the 96 well plate coated with OVA protein. Biotinylated anti-mouse IgG secondary antibody and HRP-conjugated streptavidin was used, followed by TMB substrate. The fluorescence signals were read by Bio-Rad plate reader at 550 nm wavelength and shown as mean  $\pm$  SD ( $n=8$  for no treatment and  $n=6$  for HS201-PDT group). (E) Flow cytometry analysis of T cell populations in HS201-PDT treated tumors. On day 3 post HS201-PDT treatment of E0771 tumors, mice were euthanized and tumors were harvested and digested with triple enzyme buffer. Tumor-infiltrating lymphocytes were stained with antibody cocktails, acquired by LSRII flow cytometry machine and data were analyzed by FlowJo software. PD-1 positivity and Treg population are shown as percentages for CD4 or CD8 T cells. Predictive indicators of the outcome are shown as ratios. Individual values with mean (bars) were plotted.  $n=5$  for no treatment and  $n=3$  for HS201-PDT group. (F) Abscopal effect induced by HS201-PDT. E0771 cells were implanted bilaterally to the flank of C57BL/6 mice (RT:  $1 \times 10^6$  cells/mouse, LT:  $5 \times 10^5$  cells/mouse). Tumors in right flank were treated with/without HS201-PDT 6 days after tumor cell implantation, and tumors in left flank were left untreated. The tumor growth was monitored for PDT treated side (right flank) and non-treated remote side (left flank).  $N=10$  mice for each group. Circle symbols: HS201-PDT treated mice. Square symbols: untreated mice. P value for comparison of left side tumors = 0.1031. \* $p < 0.05$ , \*\* $p < 0.01$ , \*\*\* $p < 0.001$ , \*\*\*\* $p < 0.0001$ . PDT, photodynamic therapy.

anti-PD-L1 monotherapy group showed tumor eradication during the experiment. These results suggest the synergistic effect of HS201-PDT and anti-PD-L1 in antitumor efficacy against MM3MG-HER2 tumors (figure 3D).

Based on the result of IFN- $\gamma$  ELISPOT assay, cellular immune response against HER2 extracellular domain (ECD) peptides was significantly enhanced in HS201-PDT group and combination treatment group, but not in anti-PD-L1 group compared with no treatment control group (figure 3E). Especially, the combination group showed the strongest cellular response among all groups. Corresponding to this finding, the intratumoral infiltration of CD8+T cells was significantly increased in the combination group (figure 3F). On the other hand, humoral

immune response against HER2 antigen was mildly enhanced in the anti-PD-L1 and combination treatment groups, suggesting induction of humoral immune response by these treatments (figure 3G).

To address whether tumor rejection resulted in the establishment of memory antitumor immunity in mice treated with the combination treatment, we rechallenged tumor-free mice (at least 30 days after the disappearance of tumors) by inoculating MM3MG-HER2 cells to the flank of the contralateral side. We observed no tumor growth in these mice, while most of naïve mice died within 22 days because of rapid tumor growth (figure 3H).

To confirm if the combination treatment can induce tumor antigen-specific immune response even in

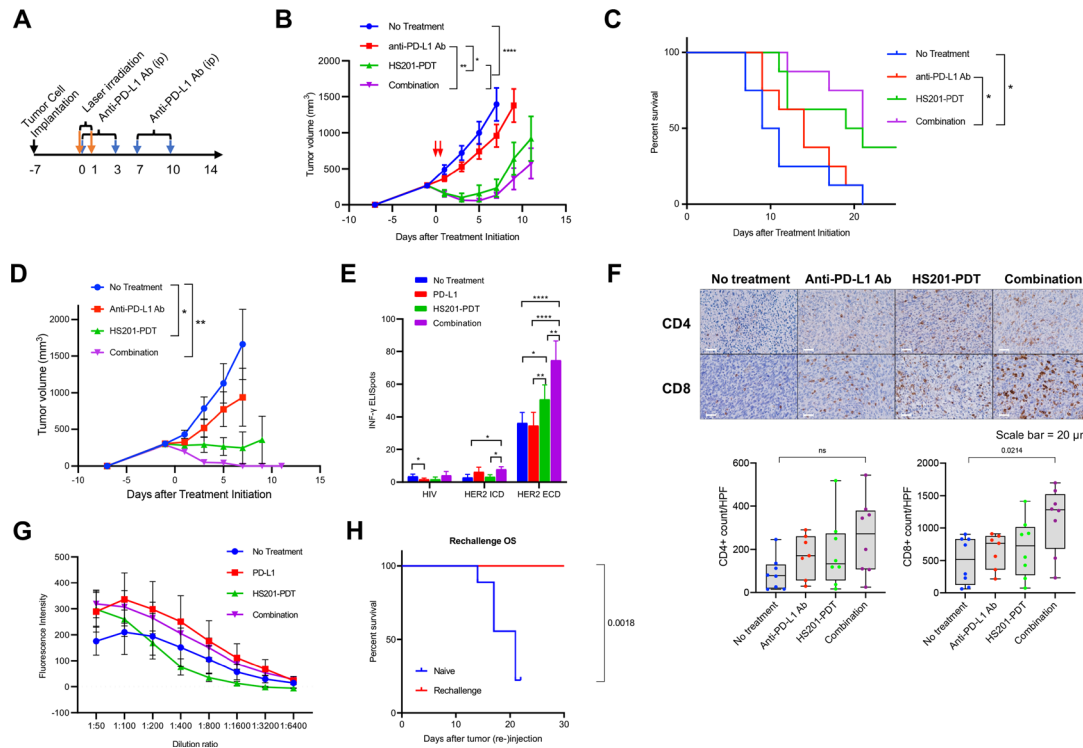


**Figure 3** Antitumor effect of HS201-PDT combined with immune checkpoint blockade against E0771 and MM3MG-HER2 breast tumors in immunocompetent mice. (A) Treatment schedule of HS201-PDT combined with Anti-PD-L1 Ab. E0771 cells were injected into right flank of female C57BL/6 mice. Mice were separated into four groups; no treatment, anti-PD-L1 Ab monotherapy, HS201-PDT monotherapy, and combination (HS201-PDT+Anti-PD-L1 Ab).  $n=8$  for each group. When the size of the tumor reached approximately 8 mm in diameter, HS201 (25 nmol/mouse) was administered to the mice via tail vein, and laser (690 nm wavelength, 120 J/cm<sup>2</sup>) was irradiated to tumor area with DLI of 6 and 24 hours in HS201-PDT monotherapy and combination groups. Anti-PD-L1 Ab (250  $\mu$ g/mouse) was injected intraperitoneally twice a week for 2 weeks in anti-PD-L1 group and combination group. (B) Antitumor effect of HS201-PDT against E0771 tumors in immunocompetent C57BL/6 mice. HS201-PDT and anti-PD-L1 Ab injection were carried out according to the schedule shown in figure 3A (laser irradiation indicated with red arrows). The data shown are mean $\pm$ SEM of tumor volumes ( $n=8$  for each group). Statistical analysis was performed for the tumor volume on day 7. (C) Survival of E0771 tumor-bearing mice treated with HS201-PDT and/or anti-PD-L1 Ab. Kaplan-Meier survival curves are shown, and log-rank test was performed for statistical analysis. Mice ( $n=8$  for each group) were counted as dead when tumor volume reached humane endpoint ( $>2000$  mm<sup>3</sup>) according to IACUC approved protocol. (D) Antitumor effect against MM3MG-HER2 tumors by HS201-PDT and/or anti-PD-L1 Ab in immunocompetent BALB/c mice. MM3MG-HER2 tumor-bearing mice were separated into four groups; no treatment, anti-PD-L1 Ab alone, HS201-PDT alone, and combination groups. After the tumors grew approximately 8 mm in diameter, HS201-PDT was performed and anti-PD-L1 Ab or control Ab was administrated intraperitoneally as described in (A). Laser irradiation is indicated with red arrows. The data shown are mean $\pm$ SEM of tumor volumes ( $n=8$  for each group). Statistical analysis was performed for the tumor volume on day 7. (E) HER2 specific T-cell response induced by treatment against MM3MG-HER2 tumor detected by ELISpot assay. Mice were sacrificed at day seven post treatment initiation for the immunoassays. HER2 peptide specific IFN- $\gamma$  production was analyzed by ELISpot assay using splenocytes. HER2 ICD or ECD peptides and HIV peptide mix were used as stimulating antigens. Results were analyzed by ELISpot reader system. ELISpot count without stimulating antigen was subtracted as a background. Data shown are mean $\pm$ SD ( $n=8$  for each group). (F) Immunohistochemical analysis of tumor-infiltrating lymphocytes. MM3MG-HER2 tumors were collected at day seven post treatment initiation. Formalin-fixed paraffin embedded tissues were cut into 4  $\mu$ m sections and stained with anti-CD4 or anti-CD8 mAb, followed by standard chromogenic immunohistochemistry protocol. Sections were counter stained with hematoxylin and eosin. Representative images from each group are shown. Original magnification: objective 40  $\times$ . The scale bar indicates 20  $\mu$ m. In the lower panels, CD4 and CD8 positive cell counts per HPF were measured using image J software and shown in box and whisker plots.  $n=7$  for anti-PD-L1,  $n=8$  for other groups. (G) Serum anti-HER2 antibody level detected by ELISA. The amount of serum antibodies specific to HER2 protein was assessed by cell-based ELISA using 4T1-HER2 and 4T1 cells. Diluted serum (1:50 to 1:6400 dilution) was added to each well confluent with cells and incubated for 1 hour on ice, then fixed with 1% formalin. IRDye 800CW anti-mouse IgG antibody was added, incubated at room temperature for 1 hour. After wash with PBS, plates were analyzed for NIR signals using LI-COR Odyssey imager at 800 nm channel. Data shown are mean $\pm$ SEM.  $n=9$  for combination group,  $n=8$  for other groups. (H) Rechallenge of tumor cells in mice treated and cured with combination treatment. At least 30 days after the disappearance of tumors in mice in combination treatment group, mice ( $n=8$ ) were rechallenged with MM3MG-HER2 tumor cells ( $5 \times 10^5$  cell number/injection) to the flank of contralateral side. As a control, naive female BALB/c mice ( $n=9$ ) received subcutaneous implantation of MM3MG-HER2 cells in the same manner. Mouse overall survival after rechallenge is shown. HPF, high-power field; PDT, photodynamic therapy; ICD, intracellular domain; ECD, extracellular domain; IACUC, Institutional Animal Care and Use Committee.

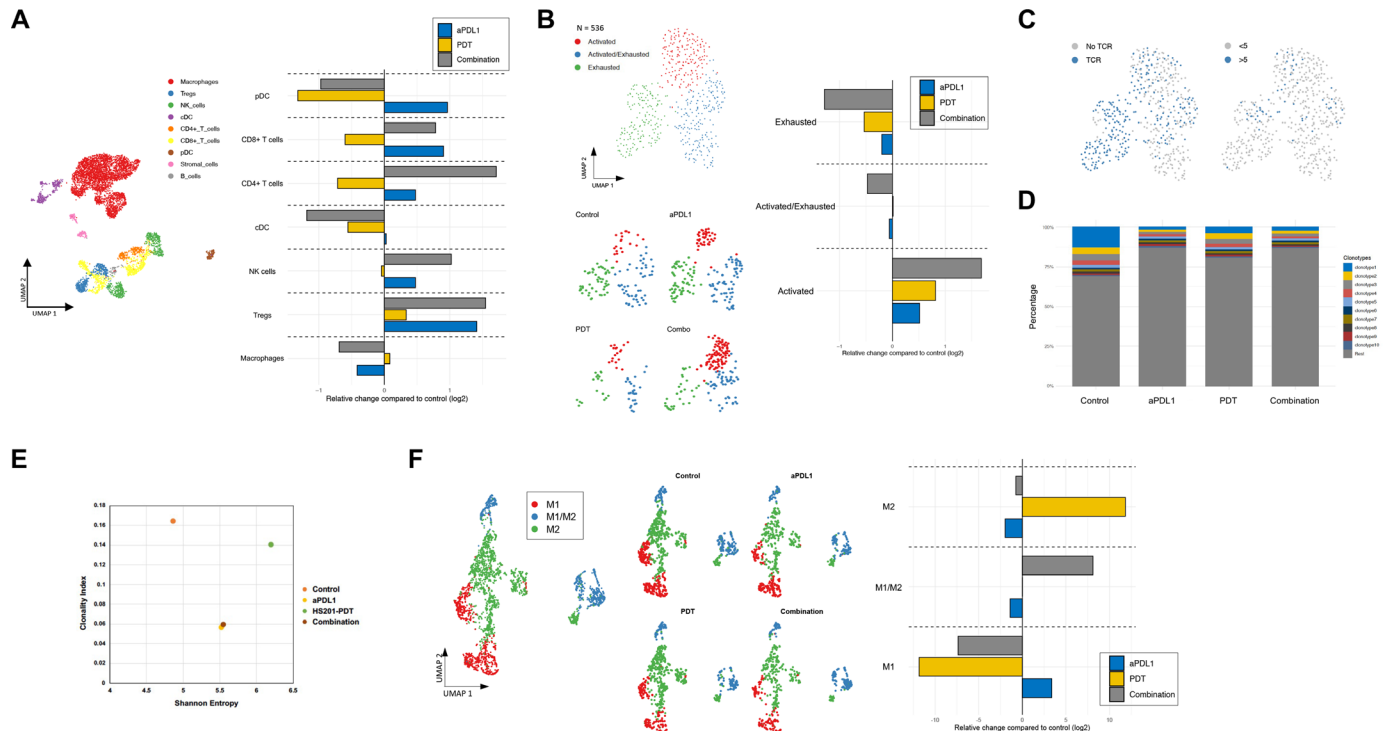


**Figure 4** scRNA-sequencing analysis of tumor-infiltrating leucocytes in treated MM3MG-HER2 tumors. (A) Changes of immune cell populations after treatments. UMAP scatter plot of single CD45+ leukocytes is shown in the left panel. Barplots in the right panel display log<sub>2</sub> expression of various immune cells across the treatment conditions relative to control samples. (B) Changes of CD8+T cell populations. Top panel displays UMAP scatter plot of single CD8+T cells labeled by their activation state. Three specific states of CD8+T cells—activated, activated/exhausted and exhausted—were identified and shown. Bottom panel shows the same separated by treatment. Barplots in the right panel display log<sub>2</sub> expression of CD8+T cells across various treatment conditions relative to control samples. (C) UMAP scatter plot of expanded CD8+T cell clones depict treatment-associated clonal expansion of activated CD8+T cells. (D) Structural organization of expanded portion of T cell repertoire. Barplots are depicting top 10 clonotypes within the expanded repertoire in each treatment Group. (E) Correlation between Shannon index and clonality index for all samples within each treatment Group. (F) UMAP scatter plot of macrophages labeled by macrophage type: M1, M1/M2 and M2. Left panel shows UMAP plot for combined cell data, while middle panel displays UMAP scatter plots for each treatment condition. Barplot in the right panel displays log<sub>2</sub> expression of macrophages across various treatment conditions relative to control samples. scRNA, single-cell RNA; UMAP, Uniform Manifold Approximation and Projection.

transgenic mice that are immune tolerant for the antigen, we used the JC-HER3 tumor model in HER3 transgenic mice (online supplemental figure 3). As we observed above, we saw the strongest antitumor efficacy and anti-HER3 cellular response in mice treated with the combination therapy, suggesting that the combination is potent enough to break immune tolerance for tumor antigens.

#### TME changes induced by anti-PD-L1, HS201-PDT and their combination

For a more detailed analyses of treatment-related changes of the tumor immune infiltrate, we used single-cell RNA sequencing of tumor infiltrating CD45+immune cells. Cell types were clustered using graph-based clustering and classified using expression of canonical cell type gene markers (figure 4A, online supplemental figure 4). Quantification of the proportions of each cell type in control and treated tumors revealed a significant increase in CD8<sup>+</sup> T cells, CD4<sup>+</sup> T cells, NK cells and Treg cells,

with a decrease in macrophages and dendritic cells in the combination-treated tumor.

GEX libraries of the CD8+T cell population were reclustered and further analyzed (figure 4B, online supplemental file 2). In addition to GEX libraries, TCR libraries were also sequenced (figure 4C). CD8+T cells were classified into activated and exhausted groups of cells based on canonical gene markers (online supplemental figure 5). Quantification of activated, activated/exhausted and exhausted CD8+T cells show a significant expansion of activated CD8+T cells in response to combination therapy. There were significantly more clones in tumors treated with combined therapy that had expanded (>5 cells sharing the same TCR, shown in blue in figure 4C) as well as significantly more unique clones present. Based on the analysis of expanding TCR clones, the top 10 clonotypes among all tumor-infiltrating T cell populations in each treatment group were identified (figure 4D). The top 10 clonotypes occupied smaller percentages of T cells in anti-PD-L1 and combination therapy groups, suggesting



increased T cell clones were generated by the treatments and infiltrated into tumors. HS201-PDT increased the diversity of T cell clones, while anti-PD-L1 and the combination treatments weakly increased the diversity and decreased clonality of T cells. Shannon index of diversity show that cells treated with anti-PD-L1 and combination treatment share a similar immune profile (figure 4E).

Similar to CD8+T cells, we explored the macrophage GEX libraries and on reclustering of these cells, we identified three groups based on canonical markers—M1, M1/M2 and M2 macrophages (online supplemental figure 6). The macrophage cell populations had differential expression patterns that correlated with treatment groups (figure 4F). There is a significant increase in M2 macrophage population post-treatment with HS201-PDT alone and M1/M2 macrophage population in combined treatment group. HS201-PDT alone and combination

treatment appeared to reduce M1 macrophage population in tumors.

Using scRNA-seq, we observed limited overlap in the genes overexpressed by intratumoral CD8+T cells in response to the monotherapies and combination. Similar results were observed in the intratumoral macrophage population. These results suggest that effects on the immune microenvironment induced by the combination are not a result of additive effects of PDT and anti-PD-L1 monotherapies, but synergistic effects (figure 5A).

We used the single cell transcriptional information to precisely map receptor-ligand interactions between CD8 T cells and macrophages. Interaction scores were computed, as previously described,<sup>31</sup> for each LR pair and compared across the various experimental conditions. The heatmap shows the cell-cell scaled communication probability of several LR along signaling pathway

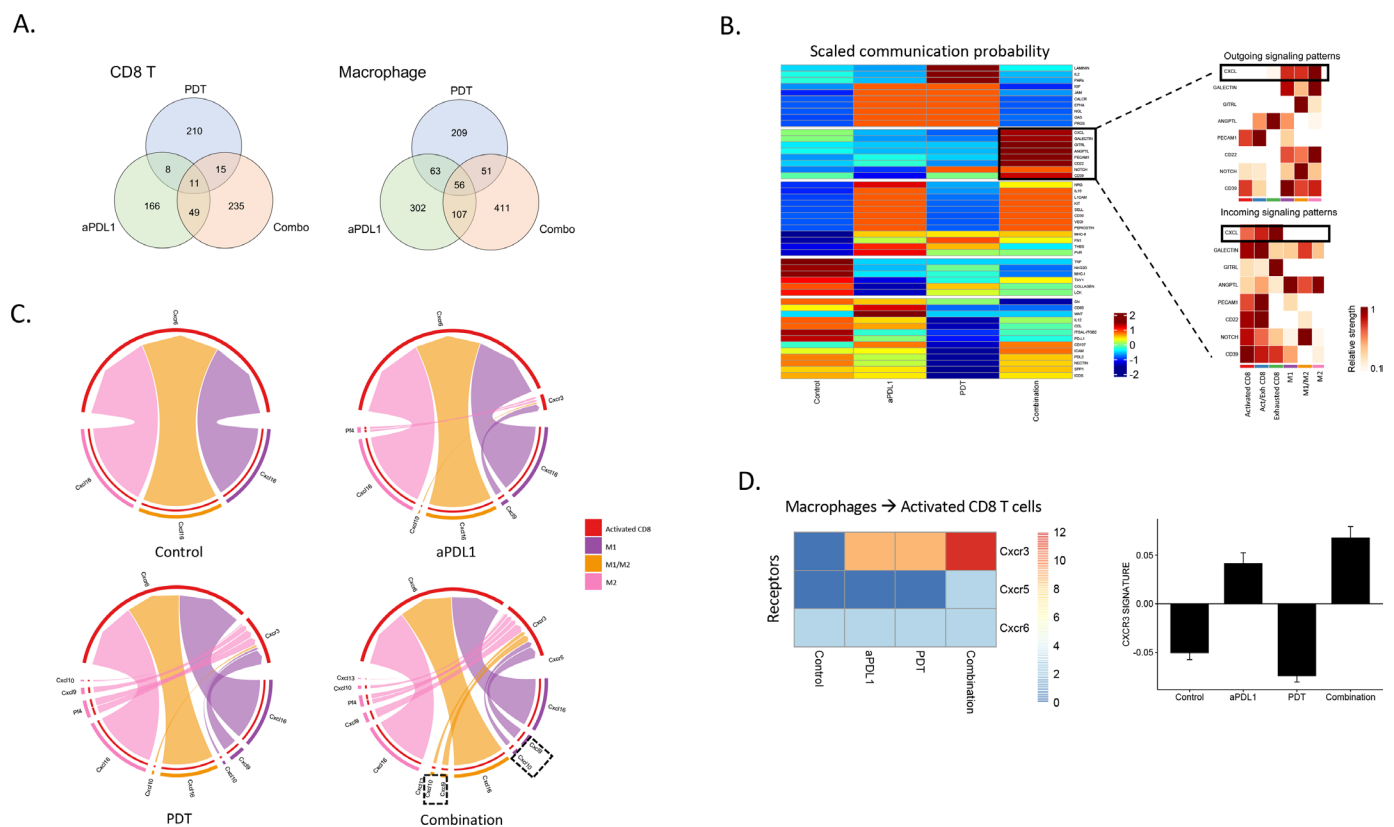


**Figure 5** Differential gene expression and changes of receptor-ligand interactions after treatments. (A) Venn diagrams show the number of differentially expressed genes (DEGs) that were upregulated in the treated samples compared with no treatment control. The number of common DEGs upregulated in multiple samples are shown in the overlapped areas. Left: CD8 T cells. Right: macrophage. (B) Heatmap showing cell-cell scaled communication probability as computed by CellChat across all treatments. Rows show signaling pathways and columns indicate average communication probability (using law of mass action by CellChat). We focus on a few signaling pathways (as shown in the solid box) for which we show heatmaps of incoming (CD8+T cells to macrophages) and outgoing (macrophages to CD8+T cells) for individual cell types. This heatmap is displaying differential number of interactions and their strength in the cell-cell communication network between control and HS201-PDT and aPD-L1 antibody combination treatment. We focus on CXCL signaling pathway because of alternating cell-cell signaling strength for incoming and out coming interactions between macrophages and CD8+T cells. (C) Chord diagrams (or circos plots) showing ligand-receptor interactions between macrophages and activated CD8+T cells in control and treatment groups. Cxcr3-associated ligand-receptor interactions are highlighted in the circos plot of the combination treatment. (D) Heatmap shows activation status of Cxcr3/Cxcr5/Cxcr6 on activated CD8+T cells in each treatment group. Enhanced CXCR3 receptor activation (due to active ligand binding from macrophages) on activated CD8+T cells is demonstrated in combination treatment group compared with others. Barplot in the right panel shows CXCR3 signature scores for each treatment group.

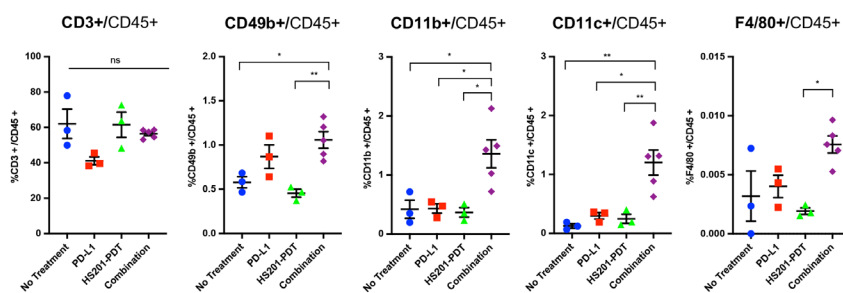
networks (figure 5B, left panel). Among pathways associated with CD8+T cell activation, CXCL, GALECTIN, GITRL, ANGPTL, PECAM1, CD22, NOTCH, and CD39 were upregulated only by the combination therapy (figure 5B, left panel). In the right panels of figure 5B, predictions of key incoming and outgoing signals for different subsets of T cells and macrophages are shown. The CXCL signaling pathway demonstrated a particularly strong cell-cell interaction between CD8+T cells and macrophages. LR interactions within the CXCL signaling pathway were visualized as a chord diagram (figure 5C) for each of the treatment groups. Although all conditions showed upregulated *Cxcr6/Cxcl16*, the CXCL9/10/11/CXCR3 axis was upregulated only in the treatment groups, and to the greatest extent in the combination treatment group. Further, the expression of *Cxcr3* on CD8 T cells was greatest in the combination treatment group (figure 5D). Expression of *Cxcl16* is expected in the TME as it is associated with M2 polarization of macrophages<sup>33</sup> and progression of BC.<sup>34</sup> Also, we have previously reported enhanced signaling of the CXCL9/10/11/CXCR3 axis as

represented by a CXCR3 gene signature to be associated with enhanced antigen presentation, T cell infiltration and expansion.<sup>19</sup> These data suggest that the combination therapy modulates the chemokine profile of the TME in a way that results in enhanced T cell infiltration.

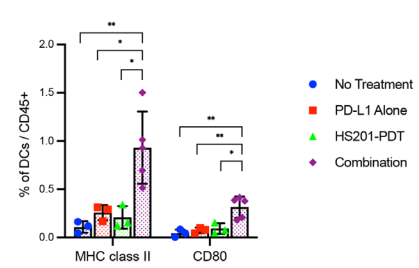
### Combination of HS201-PDT and PD-L1 blockade modulated the systemic immune profile

We also analyzed the immune profile in lymph node cells and splenocytes by flow cytometry to assess the systemic effect of combination therapy. In the lymph nodes, the relative percentages of CD11b+myeloid cells, CD49b+natural killer cells and CD11c+dendritic cells were significantly increased in the combination group (figure 6A). Dendritic cells in lymph nodes showed significantly enhanced expression of MHC class II and CD80 in the combination groups, suggesting enhanced maturation of DCs by the combination treatment (figure 6B). PD-1, ICOS, and CD69 expression on CD4+ and CD8+ splenocytes, associated with T cell activation, was significantly stronger in the combination group (figure 6C). These

#### A Immune cell populations in LNs



#### B Maturation of DCs in LNs



#### C Activation and regulatory markers in CD4 and CD8 positive splenocytes

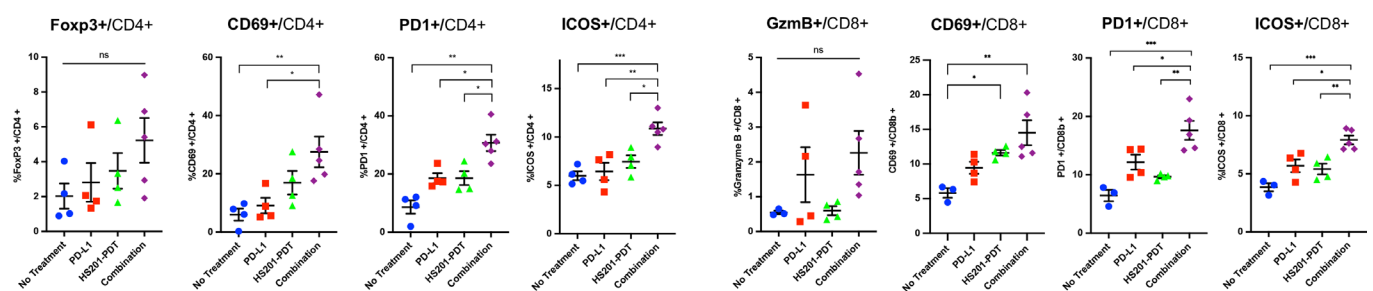


**Figure 6** Analysis of tumor-draining lymph node cells and splenocytes in MM3MG-HER2 tumor-bearing mice treated with HS201-PDT and/or anti-PD-L1 Ab. MM3MG-HER2 tumor-bearing BALB/c mice were untreated or treated with anti-PD-L1 Ab alone, HS201-PDT alone, or combination (HS201-PDT+Anti-PD-L1 Ab) when the tumor size reached approximately 8mm in diameter, on day 0, HS201 (25nmol/mouse) administration via tail vein injection was followed by the irradiation of laser (690nm wavelength, 120J/cm<sup>2</sup>) to tumor area with DLI of 6 and 24 hours. Anti-PD-L1 Ab (250µg/mouse) was administered intraperitoneally on days 0 and 3, and mice were sacrificed on day 7 post-treatment. (A) Immune cell population in tumor-draining lymph nodes. The percentages of CD3, CD49b, CD11b, CD11c and F4/80 positive cells in CD45 expressing immune cells in each treatment group are shown. The data shown are mean±SEM of percentages (n=5 for combination group and n=3 for other groups). (B) Maturation status of DCs in tumor-draining lymph nodes. CD80 and MHC class II expression by CD11c+DCs were analyzed as markers of DC maturation and shown as percentages among CD45+cells in lymph nodes. n=5 for combination group and n=3 for other groups. (C) Activation and regulatory markers in CD4/CD8 positive lymphocytes in spleen. The CD4+T cell populations expressing FOXP3, CD69, PD1, and ICOS and are shown on the left side and CD8+T cell populations expressing GzmB, CD69, PD1, and ICOS are shown on the right side. The data shown are mean±SEM of percentages (n=5 for combination group and n=4 for other groups). \*p<0.05, \*\*p<0.01, \*\*\*p<0.001. DC, dendritic cell; PDT, photodynamic therapy; ICOS, inducible costimulator; MHC, major histocompatibility complex.

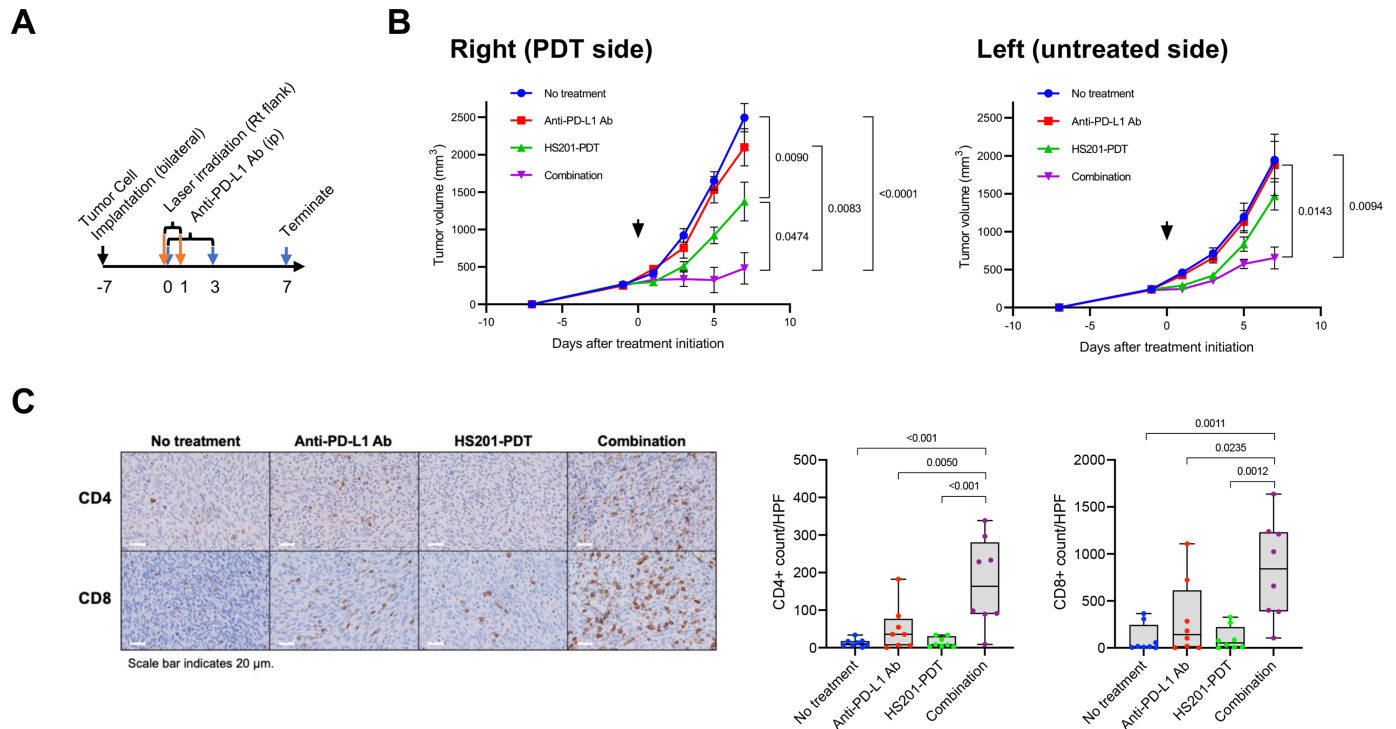


**Figure 7** Induction of stronger abscopal effect by the combination of HS201-PDT and anti-PD-L1. (A) Scheme of the treatment schedule. MM3MG-HER2 cells were subcutaneously injected to bilateral flank of female BALB/c mice. Mice were separated into four groups; no treatment, anti-PD-L1 Ab monotherapy, HS201-PDT monotherapy, and combination (HS201-PDT+Anti-PD-L1 Ab). When the tumor in the right flank grew approximately 8 mm in diameter (day 0), HS201-PDT was initiated, accompanied with intraperitoneal administration of isotype control IgG or anti-PD-L1 Ab (250  $\mu$ g/mouse) on days 0 and 3. As for the immunoassay experiment, mice were sacrificed at day seven post treatment initiation. (B) Abscopal effect induced by combination of HS201-PDT and anti-PD-L1. MM3MG-HER2 tumor cells were subcutaneously implanted to the flank bilaterally, and tumors in the right flank was treated by HS201-PDT (indicated with arrow). Average tumor volume for the right flank (PDT treated) and the left flank (untreated remote) tumors are shown for each group.  $n=8$  for each group. (C) Enhanced CD4+T and CD8+T cell infiltration in untreated remote MM3MG-HER2 tumors in mice treated with the combination of HS201-PDT and anti-PD-L1. Formalin-fixed paraffin embedded tissues were cut into 4  $\mu$ m sections and stained with anti-CD4 or anti-CD8 mAb, followed by standard chromogenic immunohistochemistry protocol. Sections were counter stained with H&E. CD4+T cells and CD8+T cells were counted in high power fields and shown in the right panel.  $n=8$  for each group. P values: \* $p<0.05$ , \*\* $p<0.01$ , \*\*\* $p<0.001$ . PDT, photodynamic therapy.

data confirm that the combination treatment caused systemic activation of CD4 and CD8 T cells.

### Combination of HS201-PDT and checkpoint blockade augmented infiltration of CD8 positive lymphocytes into distant tumors and enhanced the abscopal effect

Based on these findings of enhanced systemic tumor antigen-specific immunity by the combination treatment, we assessed whether this enhanced immunity would result in a stronger abscopal effect on the synchronous distant implanted tumors. Using the bilateral MM3MG-HER2 tumor model, we treated the right flank tumors with/without HS201-PDT and with intraperitoneal administration of anti-PD-L1 or isotype control IgG as shown in figure 7A. As previously observed, HS201-PDT treatment significantly suppressed the growth of treated tumors in the right flank compared with the no treatment control group ( $p=0.009$ ), and the combination treatment showed an even stronger antitumor effect compared with HS201-PDT alone ( $p=0.0474$ ) (figure 7B, left panel). However, HS201-PDT alone could not induce significant

tumor growth suppression of the untreated contralateral (distant) tumors, while the combination treatment significantly suppressed tumor growth of the untreated contralateral (distant) tumors compared with no treatment control (figure 6B, right panel). Immunohistochemical staining of CD4 and CD8 T cells was performed for the distant tumors, and the representative images from each treatment group are shown in figure 7C. Significantly increased infiltration of CD4 and CD8 T cells into PDT-untreated distant tumors was observed in the combination treatment group compared with other groups (right panel). These data confirm the abscopal effect is activated by the combination of HS201-PDT and anti-PD-L1 antibody.

## DISCUSSION

We have previously shown that a tumor-selective PDT (HS201-PDT) had exquisite anti-tumor efficacy across a variety of molecular and clinical subtypes of human BC

without significant systemic or local toxicity.<sup>23</sup> It has been reported that PDT as a local cancer therapy can facilitate antitumor immune responses by generating and releasing tumor-associated antigens from destroyed cancer cells, enhancing antigen presentation and cytokine/chemokine production, leading to activation of antigen-specific T cells and abscopal effects that delay the growth of distant tumors.<sup>24 25</sup> In the current study, we confirmed that HS201-PDT induced systemic antitumor immunity, greater antitumor efficacy and prolonged mouse survival in immunocompetent mice compared with immune-deficient mice, suggesting the key role of induced antitumor immunity in the treatment efficacy of HS201-PDT. We also revealed that HS201-PDT generated a more inflamed TME, associated with increased CD8/CD4 ratio and CD8/Treg ratio. Moreover, in a bilateral BC model, we confirmed the abscopal effect; however, the growth suppression of the distant implanted tumors was weak, suggesting insufficient induction of systemic antitumor immunity by HS201-PDT monotherapy. Therefore, we hypothesized that combining HS201-PDT with immunostimulatory therapies, such as microbial adjuvants, cytokine therapies or immune checkpoint inhibitors<sup>35–42</sup> would result in enhanced systemic antitumor immunity. In the current study, we observed that the combination of HS201-PDT with ICB had greater antitumor efficacy than either alone and significantly suppressed the growth of distant tumors. The mechanism for this greater activity was demonstrated to be markedly increased and matured dendritic cells in tumor draining lymph nodes, increased antigen-specific T cell activation, and T cell infiltration into both the treated and distant tumors. A novel finding was the upregulation of the CXCR3 gene signature, known to be associated with T cell activation and antigen presentation.<sup>19</sup> These results suggest that HS201-PDT combined with ICB generated an inflamed TME.

One of the major factors involved in resistance to ICB is the lack or paucity of tumor T cell infiltration, characterizing the so-called ‘cold tumors’.<sup>43 44</sup> Indeed, we observed that anti-PD-L1 alone did not significantly enhance tumor infiltration of CD8+T cells and did not suppress tumor growth; however, the infiltration of activated CD4+and CD8+ T cells was increased and exhausted CD8+T cells was decreased in the treated tumor by the combination treatment, associated with greater tumor growth suppression in our HER2+BC model. Further, we confirmed that the combination treatment could potently suppress the growth of tumors in distant sites with an apparent increase of infiltrating CD4+and CD8+ T cells. Therefore, we conclude that HS201-PDT has a strong potential to maximize the efficacy of ICB treatment, by turning cold tumor to hot, and can exert synergistic effects with anti-PD-L1 antibody to enhance the antitumor efficacy in these BC models.

To elucidate the detailed mechanism of increased infiltration of tumor with activated T cells and enhanced antitumor efficacy of the combination treatment compared with anti-PD-L1 or HS201-PDT monotherapy, the TME

was assessed by scRNA-seq analysis, which revealed that the combination treatment induced the increase of T cell clones and TCR repertoire diversity in MM3MG-HER2 tumors. Importantly, the T cell response was antigen-specific and the combination treatment could break tolerance to the tumor antigen HER3 in immune-tolerant HER3-transgenic mice implanted with JC-HER3 tumor. Increased TCR diversity of TILs has been reported for other immunotherapeutic interventions for cancers, such as sipuleucel-T treatment for prostate cancer patients,<sup>45</sup> and also was demonstrated to be associated with improved overall survival of patients with various types of cancers, including BC, melanoma, squamous lung carcinoma, clear cell renal carcinoma and testicular cancer.<sup>46</sup> Interestingly, in the current study, all treatment groups, especially those with HS201-PDT treatment, showed increased TCR diversity compared with the no treatment control, suggesting HS201-PDT treatment increases T cell populations that can recognize tumor-specific antigens and target tumor cells.

RNA-seq data also demonstrated that the combination strategy of HS201-PDT with ICB enhanced expression of the CXCR3 gene signature in TILs, confirming the importance of CXCL9/10 ligand- CXCR3 receptor interactions between macrophages and CD8 T cells for the activation of antitumor immunity in response to immune checkpoint inhibitors in our HER2+BC model. The CXCL9/10/11/CXCR3 axis has been studied extensively in melanoma as a potential prognostic biomarker for improved clinical outcomes and a potential predictive biomarker for responses to immune checkpoint inhibitors.<sup>10 47</sup> We recently reported an enhanced signaling of CXCL9/10/11/CXCR3 axis in the TME of TNBC after intratumoral IL-12 gene therapy.<sup>19</sup> The CXCR3 gene signature was associated with enhanced antigen presentation, T cell infiltration and expansion in the TME. Further, analysis of a genomic database demonstrated that the expression of our CXCR3 gene signature was associated with improved disease-free survival and overall survival in patients with TNBC.<sup>19</sup> In TNBC and melanoma models, the macrophage derived CXCR3 ligands, CXCL9 and CXCL10, were upregulated following dual PD-1/CTLA-4 blockade, and played pivotal roles in CD8+T cell infiltration and therapeutic efficacy of ICB.<sup>48</sup>

Other preclinical studies have demonstrated that the combination of PDT and immune checkpoint inhibitors, such as anti-CTLA-4 or anti-PD-1 antibodies, significantly improved therapeutic efficacy and survival of mice in murine models of colorectal cancer and BC.<sup>41 49</sup> Similar to our observation, the combination with anti-PD-1 antibody induced maturation of dendritic cells in tumor draining lymph nodes and enhanced the recruitment of cytotoxic CD8+T cells to the tumors in a 4T1 BC model<sup>49</sup>; however, this study did not describe a detailed analysis of the immune environment of treated tumors or distant TME and did not report the antigen-specificity of the induced immune response.

For the implementation of this novel combination strategy in patients with BC, we acknowledge the limitation due to the modest tissue penetration of laser light, especially when targeted tumors are located deep in the visceral organs. Thus, clinical trials of PDT for BC have been conducted mostly for chest wall recurrence of BC, that showed excellent clinical responses.<sup>50</sup> Interestingly, a recent study reported percutaneous transcatheter insertion of an optic fiber cable into tumors to deliver laser light directly, which induced tumor necrosis,<sup>51</sup> suggesting a possible approach for delivering light to tumors in deeper locations, such as visceral organs or bones. The abscopal effect caused by our combination strategy would then allow us to treat synchronous distant tumors by applying PDT to a single tumor nodule using an optimal approach for each case, such as surface, endoscopic or transcatheter laser exposure.

Another potential criticism for our current study is that we only evaluated the PDT effect on superficial tumors that grew after subcutaneous implantation of tumor cells, and no analyses were done using optimized spontaneously metastasizing models. In previously published preclinical studies,<sup>52–53</sup> however, the combination of PDT and anti-PD-L1 was shown to suppress lung metastasis of 4T1 tumors, while PDT or anti-PD-L1 itself did not. Unfortunately, in the BC models used in our study, primary tumors grew rapidly to reach humane endpoints before causing analyzable visceral organ metastases. In our next study, we plan to test if HS201-PDT can suppress the spontaneous metastases to the visceral organs using optimal BC models.

In summary, our current study demonstrated that HS201-PDT combined with PD-L1 blockade could elicit remarkable antigen specific antitumor immunity that can exert striking therapeutic effects against PDT-treated and synchronous distant tumors in BC models. These results warrant the clinical testing of HS201-PDT combined with PD-1/PD-L1 blockade in patients with BC. Cxcr3 signaling may serve as a surrogate marker for clinical activity of this strategy.

**Acknowledgements** We thank Tao Wang for her technical assistance in flow cytometry.

**Contributors** KK, HKL and TO designed the study. KK, HN, XY and TO performed the experiments. KK, CRA, HN, ZCH, AH and TO analyzed the data. PFH and TAJH developed and supplied materials used in the experiment. KK, MAM, HKL and TO wrote the paper. TO is a guarantor for this study and publication.

**Funding** This research was supported by DOD TVA W81XWH-12-1-0447 Grant No. BC111085.

**Competing interests** Molecules discussed in this manuscript are covered under an issued patent (US9,738,643B2) filed by Duke University.

**Patient consent for publication** Not applicable.

**Ethics approval** Not applicable.

**Provenance and peer review** Not commissioned; externally peer reviewed.

**Data availability statement** Data are available on reasonable request. Data relevant to the study are included in the article or available on reasonable request to the correspondence author.

**Supplemental material** This content has been supplied by the author(s). It has not been vetted by BMJ Publishing Group Limited (BMJ) and may not have been peer-reviewed. Any opinions or recommendations discussed are solely those of the author(s) and are not endorsed by BMJ. BMJ disclaims all liability and responsibility arising from any reliance placed on the content. Where the content includes any translated material, BMJ does not warrant the accuracy and reliability of the translations (including but not limited to local regulations, clinical guidelines, terminology, drug names and drug dosages), and is not responsible for any error and/or omissions arising from translation and adaptation or otherwise.

**Open access** This is an open access article distributed in accordance with the Creative Commons Attribution Non Commercial (CC BY-NC 4.0) license, which permits others to distribute, remix, adapt, build upon this work non-commercially, and license their derivative works on different terms, provided the original work is properly cited, appropriate credit is given, any changes made indicated, and the use is non-commercial. See <http://creativecommons.org/licenses/by-nc/4.0/>.

#### ORCID iDs

Chaitanya R Acharya <http://orcid.org/0000-0001-7149-1749>

Zachary Conrad Hartman <http://orcid.org/0000-0001-6549-8207>

Herbert Kim Lyerly <http://orcid.org/0000-0002-0063-4770>

Takuya Osada <http://orcid.org/0000-0003-1424-5001>

#### REFERENCES

- Henriques B, Mendes F, Martins D. Immunotherapy in breast cancer: when, how, and what challenges? *Biomedicine* 2021;9:1687.
- Tavares DF, Ribeiro C V, Andrade MAV, Rhangel Gomes Teixeira T, Ramos Varrone G, Lopes Britto R. Immunotherapy using PD-1/PDL-1 inhibitors in metastatic triple-negative breast cancer: a systematic review. *Oncol Rev* 2021;15:497.
- Tolba MF, Omar HA. Immunotherapy, an evolving approach for the management of triple negative breast cancer: converting non-responders to responders. *Crit Rev Oncol Hematol* 2018;122:202–7.
- Mohan N, Hosain S, Zhao J, et al. Atezolizumab potentiates Tcell-mediated cytotoxicity and coordinates with FAK to suppress cell invasion and motility in PD-L1<sup>+</sup> triple negative breast cancer cells. *Oncoimmunology* 2019;8:e1624128.
- Schmid P, Adams S, Rugo HS, et al. Atezolizumab and nab-paclitaxel in advanced triple-negative breast cancer. *N Engl J Med* 2018;379:2108–21.
- Fan Y, He S. The characteristics of tumor microenvironment in triple negative breast cancer. *Cancer Manag Res* 2022;14:1–17.
- Thomas R, Al-Khadairi G, Decock J. Immune checkpoint inhibitors in triple negative breast cancer treatment: promising future prospects. *Front Oncol* 2020;10:600573.
- Tannenbaum CS, Tubbs R, Armstrong D, et al. The CXC chemokines IP-10 and mig are necessary for IL-12-mediated regression of the mouse RENCA tumor. *J Immunol* 1998;161:927–32.
- Harlin H, Meng Y, Peterson AC, et al. Chemokine expression in melanoma metastases associated with CD8<sup>+</sup> T-cell recruitment. *Cancer Res* 2009;69:3077–85.
- Tokunaga R, Zhang W, Naseem M, et al. CXCL9, CXCL10, CXCL11/CXCR3 axis for immune activation - A target for novel cancer therapy. *Cancer Treat Rev* 2018;63:40–7.
- Liang Y-K, Deng Z-K-, Chen M-T, et al. Cxcl9 is a potential biomarker of immune infiltration associated with favorable prognosis in ER-negative breast cancer. *Front Oncol* 2021;11:710286.
- Pandey V, Fleming-Martinez A, Bastea L, et al. CXCL10/CXCR3 signaling contributes to an inflammatory microenvironment and its blockade enhances progression of murine pancreatic precancerous lesions. *Elife* 2021;10:e60646.
- Oghumu S, Varikuti S, Terrazas C, et al. CXCR3 deficiency enhances tumor progression by promoting macrophage M2 polarization in a murine breast cancer model. *Immunology* 2014;143:109–19.
- Ledys F, Kalfest L, Galland L, et al. Therapeutic associations comprising anti-PD-1/PD-L1 in breast cancer: clinical challenges and perspectives. *Cancers* 2021;13:5999.
- Amouzegar A, Chelvanambi M, Filderman JN, et al. Sting agonists as cancer therapeutics. *Cancers* 2021;13:2695.
- Probst U, Fuhrmann I, Beyer L, et al. Electrochemotherapy as a new modality in interventional oncology: a review. *Technol Cancer Res Treat* 2018;17:1533033818785329.
- Malvey J, Samoylenko I, Schadendorf D, et al. Talimogene laherparepvec upregulates immune-cell populations in non-injected lesions: findings from a phase II, multicenter, open-label study in patients with stage IIIB-IVM1c melanoma. *J Immunother Cancer* 2021;9.

- 18 Rhines LD, Sampath P, DiMeco F, *et al.* Local immunotherapy with interleukin-2 delivered from biodegradable polymer microspheres combined with interstitial chemotherapy: a novel treatment for experimental malignant glioma. *Neurosurgery* 2003;52:872–80.
- 19 Telli ML, Nagata H, Wapnir I, *et al.* Intratumoral Plasmid IL12 Expands CD8<sup>+</sup> T Cells and Induces a CXCR3 Gene Signature in Triple-negative Breast Tumors that Sensitizes Patients to Anti-PD-1 Therapy. *Clin Cancer Res* 2021;27:2481–93.
- 20 Eranki A, Srinivasan P, Ries M, *et al.* High-Intensity focused ultrasound (HIFU) triggers immune sensitization of refractory murine neuroblastoma to checkpoint inhibitor therapy. *Clin Cancer Res* 2020;26:1152–61.
- 21 Balakrishnan PB, Sweeney EE, Ramanujam AS, *et al.* Photothermal therapies to improve immune checkpoint blockade for cancer. *Int J Hyperthermia* 2020;37:34–49.
- 22 Abe S, Nagata H, Crosby EJ, *et al.* Combination of ultrasound-based mechanical disruption of tumor with immune checkpoint blockade modifies tumor microenvironment and augments systemic antitumor immunity. *J Immunother Cancer* 2022;10:e003717.
- 23 Kaneko K, Osada T, Morse MA, *et al.* Heat shock protein 90-targeted photodynamic therapy enables treatment of subcutaneous and visceral tumors. *Commun Biol* 2020;3:226.
- 24 Castano AP, Mroz P, Hamblin MR. Photodynamic therapy and anti-tumour immunity. *Nat Rev Cancer* 2006;6:535–45.
- 25 Mroz P, Szokalska A, Wu MX, *et al.* Photodynamic therapy of tumors can lead to development of systemic antigen-specific immune response. *PLoS One* 2010;5:e15194.
- 26 Osada T, Kaneko K, Gwin WR, *et al.* *In Vivo* Detection of HSP90 Identifies Breast Cancers with Aggressive Behavior. *Clin Cancer Res* 2017;23:7531–42.
- 27 Osada T, Morse MA, Hobeika A, *et al.* Vaccination targeting human HER3 alters the phenotype of infiltrating T cells and responses to immune checkpoint inhibition. *Oncoimmunology* 2017;6:e1315495.
- 28 Johnstone CN, Smith YE, Cao Y, *et al.* Functional and molecular characterisation of EO771.LMB tumours, a new C57BL/6-mouse-derived model of spontaneously metastatic mammary cancer. *Dis Model Mech* 2015;8:237–51.
- 29 Stuart T, Butler A, Hoffman P, *et al.* Comprehensive integration of single-cell data. *Cell* 2019;177:1888–902.
- 30 Becht E, McInnes L, Healy J, *et al.* Dimensionality reduction for visualizing single-cell data using UMAP. *Nat Biotechnol* 2019;37:38–44.
- 31 Jin S, Guerrero-Juarez CF, Zhang L, *et al.* Inference and analysis of cell-cell communication using CellChat. *Nat Commun* 2021;12:1088.
- 32 Shannon CE. A mathematical theory of communication. *Bell System Technical Journal* 1948;27:379–423.
- 33 Cho SW, Kim YA, Sun HJ, *et al.* CXCL16 signaling mediated macrophage effects on tumor invasion of papillary thyroid carcinoma. *Endocr Relat Cancer* 2016;23:113–24.
- 34 Mir H, Kapur N, Gales DN, *et al.* CXCR6-CXCL16 axis promotes breast cancer by inducing oncogenic signaling. *Cancers* 2021;13:3568.
- 35 Myers RC, Lau BH, Kunihira DY, *et al.* Modulation of hematoporphyrin derivative-sensitized phototherapy with *Corynebacterium parvum* in murine transitional cell carcinoma. *Urology* 1989;33:230–5.
- 36 Korbek M, Sun J, Posakony JJ. Interaction between photodynamic therapy and BCG immunotherapy responsible for the reduced recurrence of treated mouse tumors. *Photochem Photobiol* 2001;73:403–9.
- 37 Korbek M, Cecic I. Enhancement of tumour response to photodynamic therapy by adjuvant Mycobacterium cell-wall treatment. *J Photochem Photobiol B* 1998;44:151–8.
- 38 Uehara M, Sano K, Wang ZL, *et al.* Enhancement of the photodynamic antitumor effect by streptococcal preparation OK-432 in the mouse carcinoma. *Cancer Immunol Immunother* 2000;49:401–9.
- 39 Bellnier DA. Potentiation of photodynamic therapy in mice with recombinant human tumor necrosis factor- $\alpha$ . *J Photochem Photobiol B* 1991;8:203–10.
- 40 Gotab J, Wilczyński G, Zagodzón R, *et al.* Potentiation of the anti-tumour effects of Photofrin-based photodynamic therapy by localized treatment with G-CSF. *Br J Cancer* 2000;82:1485–91.
- 41 Yuan Z, Fan G, Wu H, *et al.* Photodynamic therapy synergizes with PD-L1 checkpoint blockade for immunotherapy of CRC by multifunctional nanoparticles. *Mol Ther* 2021;29:2931–48.
- 42 Kleinovink JW, Fransen MF, Löwik CW, *et al.* Photodynamic-Immune Checkpoint Therapy Eradicates Local and Distant Tumors by CD8<sup>+</sup> T Cells. *Cancer Immunol Res* 2017;5:832–8.
- 43 Tumeah PC, Harview CL, Yearley JH, *et al.* PD-1 blockade induces responses by inhibiting adaptive immune resistance. *Nature* 2014;515:568–71.
- 44 McDermott DF, Huseni MA, Atkins MB, *et al.* Clinical activity and molecular correlates of response to atezolizumab alone or in combination with bevacizumab versus sunitinib in renal cell carcinoma. *Nat Med* 2018;24:749–57.
- 45 Sheikh N, Cham J, Zhang L, *et al.* Clonotypic diversification of intratumoral T cells following Sipuleucel-T treatment in prostate cancer subjects. *Cancer Res* 2016;76:3711–8.
- 46 Valpione S, Mundra PA, Galvani E. The T cell receptor repertoire of tumor infiltrating T cells is predictive and prognostic for cancer survival. Erratum in: *Nat Commun*. 2021 Jul 22;12(1):4588. *Nat Commun* 2021;12:4098.
- 47 Bridge JA, Lee JC, Daud A, *et al.* Cytokines, chemokines, and other biomarkers of response for checkpoint inhibitor therapy in skin cancer. *Front Med* 2018;5:351.
- 48 House IG, Savas P, Lai J, *et al.* Macrophage-Derived CXCL9 and CXCL10 are required for antitumor immune responses following immune checkpoint blockade. *Clin Cancer Res* 2020;26:487–504.
- 49 Gao L, Zhang C, Gao D, *et al.* Enhanced anti-tumor efficacy through a combination of integrin  $\alpha$ v $\beta$ 6-Targeted photodynamic therapy and immune checkpoint inhibition. *Theranostics* 2016;6:627–37.
- 50 Morrison SA, Hill SL, Rogers GS, *et al.* Efficacy and safety of continuous low-irradiance photodynamic therapy in the treatment of chest wall progression of breast cancer. *J Surg Res* 2014;192:235–41.
- 51 Banerjee SM, El-Sheikh S, Malhotra A, *et al.* Photodynamic therapy in primary breast cancer. *J Clin Med* 2020;9:483.
- 52 Duan X, Chan C, Guo N, *et al.* Photodynamic therapy mediated by nontoxic core-shell nanoparticles synergizes with immune checkpoint blockade to elicit antitumor immunity and antimetastatic effect on breast cancer. *J Am Chem Soc* 2016;138:16686–95.
- 53 Chen Z, Liu L, Liang R, *et al.* Bioinspired hybrid protein oxygen nanocarrier amplified photodynamic therapy for eliciting anti-tumor immunity and Abscopal effect. *ACS Nano* 2018;12:8633–45.